scientific reports

Check for updates

OPEN

Influence of coriolis force and nanoparticle aggregation on entropy generation and thermal conductivity in dusty nanofluid flow: a numerical investigation

Bagh Ali[1], Muzammil Hussain[2], Aziz Ullah Awan[2,3], N. Ameer Ahammad[4], Fehmi Gamaoun [5], Daba Meshesha Gusu[6]✉ & Sohail Nadeem[7]

The present research introduces a novel framework for analyzing dusty nanofluid flow within a rotating frame, emphasizing the combined influence of nanoparticle aggregation, viscous dissipation, radiation, porous medium effects, and Coriolis force. The study's novelty lies in integrating these coupled mechanisms with entropy generation analysis to provide a unified thermofluid model. This model offers fresh insights into how radiation-rotation coupling, aggregation, and porous resistance reshape momentum and thermal transport in dusty nanofluid systems. The governing partial differential equations are transformed into nonlinear ordinary differential equations using similarity variables and solved numerically via MATLAB's bvp4c solver. Validation is established by comparing the results with published studies for limiting cases. The findings indicate that while aggregation reduces velocity, it increases the Nusselt number and temperature. Coriolis forces increase transverse flow and thicken the thermal layer, while radiation increases temperature and heat transfer but diminishes the axial flow. Aggregation lowers the Nusselt and Bejan numbers by about 20% and 15%, respectively. These results provide practical insights for the design of thermal management and nuclear cooling systems, rotating thermal-fluid systems such as filtration processes, aerosol technology, rotating energy devices, and environmental engineering applications.

Keywords Dusty fluid, Entropy generation, Darcy–Forchheimer porous medium, Rotating frame, Nanoparticle aggregation, Numerical scheme

List of symbols

Roman symbols

$(\check{x}, \check{y}, \check{z})$	Cartesian coordinates, m
$(\check{v}_1, \check{v}_2, \check{v}_3)$	Velocity components, m/s
$(\check{v}_{1p}, \check{v}_{2p}, \check{v}_{3p})$	Dust-phase velocity components, m/s
K_0	Permeability of porous medium, m^2
$\check{T}$	Temperature, K
$\check{T}_\infty$	Ambient temperature, K
c_p	Specific heat, J/kg K
C_b	Drag coefficient, –
m^*	Mean absorption coefficient, m^{-1}
F^*	Non-uniform inertia coefficient, –

[1]Department of Mathematical Sciences, Saveetha School of Engineering, SIMATS, Chennai, Tamilnadu 602105, India. [2]Institute of Mathematics, University of the Punjab, Lahore 54590, Pakistan. [3]Center for Theoretical Physics, Khazar University, 41 Mehseti Str., AZ1096 Baku, Azerbaijan. [4]Department of Mathematics, Faculty of Science, University of Tabuk, 71491 Tabuk, Saudi Arabia. [5]Department of Mechanical Engineering, College of Engineering, King Khalid University, 61421 Abha, Saudi Arabia. [6]Department of Mathematics, College of Natural and Computational Sciences, Ambo University, Ambo, Ethiopia. [7]Department of Mathematics, Quaid-i-Azam University, Islamabad 45320, Pakistan. ✉email: daba.meshesha@ambou.edu.et

K	Stokes' drag constant, –
Nu_x	Local Nusselt number, –
Cf_x	Local skin friction coefficient, –
E_{gen}	Volumetric entropy generation rate, W/m^3 K
E_0	Characteristic entropy rate, W/m^3 K

Greek symbols

α_1^*	Stefan–Boltzmann constant, W/m^2 K^4
η	Similarity variable, –
Ω	Angular velocity, rad/s
Γ_r	Rotation parameter, –
θ, θ_p	Dimensionless temperature profiles, –

Dimensionless numbers

Br	Brinkman number, –
P_r	Prandtl number, –
Rd	Radiation parameter, –
E_c	Eckert number, –
F_r	Forchheimer number, –
(F', F_p, G, G_p)	Dimensionless velocity profiles, –
Ns	Entropy generation number, –
Be	Bejan number, –

Dusty fluid flow occurs when solid dust particles are distributed throughout a fluid medium. During fluidization process, chemical reactions facilitate the formation of raindrops by interacting with the dusty air and dispersing tiny particles in the fluid. This phenomenon has numerous uses, including paint spraying, nuclear reactor cooling systems, biomedical technologies, and precise guiding systems. Saffman[1] established the concept of dusty fluids and developed constitutive equations using Stokes' law of drag. His research found that including dust particles in a fluid enhances the thermal transfer rate. Ezzat et al.[2] investigated the free-convective heat transfer in a dusty fluid flow caused by a vertical plate in a permeable medium with an applied magnetic field. Dey and Chutia[3] analyzed bioconvective dusty nanofluid flow over a vertically extended flat surface. Sharif et al.[4] conducted numerical research on trihybrid Ellis dusty nanofluid flow through an expanding Riga plate. Examining dusty flow mechanisms helps understanding thermodynamic losses, such as entropy formation, in these systems.

Entropy generation, a fundamental thermodynamic term, quantifies irreversibility and disorder in energy transfer. Entropy generation minimization is crucial in solar energy, electronics, and heat exchangers. Bejan[5–7] developed the concept of entropy optimization for mass and heat transfer phenomena. Kumar et al.[8] examined entropy generation in hybrid nanofluids inside porous medium with viscous dissipation, Joule heating, and radiation, while Agrawal and Kaswan[9] looked at how entropy is generated in nanofluids. Khan et al.[10] investigated nanofluid flow across a curved, stretchy sheet, including heat and mass transfer and entropy generation. Kumar et al.[11,12] employed Darcy–Forchheimer models to look at entropy production, convective heat, and mass transfer in nanofluids. Yusuf et al.[13] studied entropy generation to evaluate thermodynamic efficiency of nanofluid-assisted enhanced oil recovery. This thermodynamic viewpoint inherently applies to nanofluid research, in which nanoparticle dispersion significantly affects entropy and heat transfer[14].

Choi and Eastman[15] developed the concept of distributing nanoparticles into base fluids to improve thermal conductivity. Incorporation of nanoparticles into base fluids increases heat transfer performance and has many applications[16,17]. Darvesh et al.[18] conducted a computational analysis of mixed convective flow of a variable-viscosity Cross nanofluid over a dynamic permeable surface, considering thermal radiation and an inclined magnetic field. Abbas et al.[19] investigated the Buongiorno model for incompressible, time-independent Sutterby fluid flow on a nonlinear stretching cylinder. Shah et al.[20] explored how ternary hybrid nanofluids influence blood velocity and heat transfer in stenosed arteries. Recent work on nanofluids may be found in[21–23]. The efficiency of these nanofluids is contingent upon particle interaction events, including aggregation and clustering.

Studying nanoparticle aggregation is critical because it directly influences the performance and usefulness of nanofluids in various advanced applications. Controlled aggregation improves heat transport, stability, and material characteristics, but excessive clustering causes sedimentation and inefficiency. In biological applications, it determines biodistribution and safety, whereas in material production, it affects uniformity and performance. Aggregation can be tailored for various applications by modifying the surface or adding stabilizers. Experimental studies[25,26] show that nanoparticle aggregation considerably improves the heat transfer properties of nanofluids. Wang et al.[27] found that particle clustering significantly improves thermal conductivity of nanofluids. The Coriolis force makes these interactions between particles and fluids much more complicated, affecting both the stability of the flow and the way heat moves through it.

The analysis of fluid flow in rotating systems is crucial across numerous engineering and industrial applications. The Coriolis force fundamentally influences the dynamics. This force is a pivotal factor in systems like vacuum pumps and motors prompting academics to comprehend their underlying science better. The studies by Liu et al.[28] on friction stir welding and by Ali et al.[30] on Maxwell fluid within a cylinder inherently involve Coriolis-driven flow modifications. Similarly, the impact of this force was explicitly examined by Bilal and Ramzan[29] within porous media. Mishra and Mondal[31] studied a spinning nanofluid under Coriolis and Lorentz forces on a vertically moving plate.

Novelty and significance of the study

The existing literature shows that three-dimensional radiative dusty nanofluid flow within a Darcy–Forchheimer porous medium remains largely unexplored. prior research has primarily concentrated on either nanofluid or

Authors	Dusty fluid	Nanofluid	Aggregation	Radiation	Rotating flow	Porous media	Entropy analysis
Jat et al.[32]	✗	✓	✗	✓	✗	✓	✗
Shaheen et al.[33]	✓	✓	✗	✓	✗	✓	✗
Jat et al.[34]	✗	✗	✗	✓	✗	✓	✓
Seth et al.[35]	✗	✓	✗	✗	✓	✓	✓
Tlili et al.[36]	✓	✓	✗	✓	✗	✓	✓
Yusuf et al.[37]	✗	✓	✗	✓	✗	✗	✓
Present study	✓	✓	✓	✓	✓	✓	✓

Table 1. Identified research gaps and novelty of the present study.

Material	Density ρ (kg/m^3)	Specific heat c_p (J/kg K)	Thermal conductivity κ (W/m K)
Water (H_2O)	991.1	4179.0	0.613
TiO_2	4250.0	686.2	8.9538

Table 2. Thermophysical characteristics of base fluid (H_2O) and nanoparticles (TiO_2)[42–44].

dusty fluid in isolation, neglecting the synergistic effects that occur when particle dynamics, radiation, and porous resistance operate simultaneously under rotational motion. The research gap is identified in Table 1. The gap is addressed in this work by formulating a rotating dusty nanofluid model that accounts for thermal radiation, viscous dissipation, nanoparticle aggregation, and Coriolis forces. Both homogeneous and aggregation-based nanoparticle models are utilized to capture realistic behavior. Furthermore, This study extends beyond conventional models by incorporating entropy generation, thereby linking heat transmission behavior with energy efficiency and irreversibility. The novelty of this work lies in:

- Developing a comprehensive framework for three-dimensional rotating dusty nanofluid flow through a Darcy–Forchheimer porous medium.
- Studying the role of the Coriolis force, viscous dissipation, and nonlinear radiation in dusty fluid flow.
- Examining the interactive roles of nanoparticle aggregation and porous resistance on thermal and momentum transport.
- Performing entropy generation analysis to measure irreversibility and assess energy efficiency in thermal-fluid systems.
- Emphasizing the importance of effective nanofluid properties through the Tiwari-Das model to better represent the physical response of nanoparticle suspensions.

This study is important because it looks at these coupled mechanisms, which give us a better idea of how dusty nanofluids move in rotating industrial and environmental systems. The findings have immediate ramifications for the enhancement of engineering processes, including rotating heat exchangers, filtration and cooling apparatus, and aerosol-based systems, where dust accumulation, nanoparticle aggregation, and rotation dictate system efficacy. This study fills a gap in the research and helps make energy use more efficient, cut down on entropy generation, and better control heat and momentum management in porous rotating systems.

Research objectives

The purpose of this article is to address the following research questions:

- How does nanoparticle aggregation affect effective heat transfer?
- How does Coriolis force impact the thermal and momentum profiles for both fluid and dust phases, with and without nanoparticle aggregation?
- What effects do rotation and porosity have on the motion of the nanofluid in axial and transverse directions?
- How is the temperature of dusty nanofluid affected by the porosity, Forchheimer number, and radiation parameter?
- How can entropy production be optimized?

Flow analysis and mathematical modeling

This study investigates the steady, three-dimensional flow of dusty radiative rotating nanofluid induced by a stretching sheet in a porous medium. The work focuses on minimizing entropy generation in dusty nanofluid flow. Adding TiO_2 nanoparticles to water greatly increases its ability to conduct heat and transfer heat through convection, making it a very efficient nanofluid. This enhanced fluid is crucial for solar energy collectors and microelectronics thermal management, where rapid heat dissipation and efficient energy transport are required. Table 2 presents the thermophysical characteristics of base fluid (water) and nanoparticle (TiO_2).

The following physical assumptions are considered for the flow problem:

- The flow inside the porous media is described using the Darcy–Forchheimer model.

- Radiation and viscous dissipation effects are incorporated.
- The surface lies in the $\check{x}\check{y}$-plane of a Cartesian coordinate system, with fluid occupying the region $\check{z} \geq 0$.
- The surface has constant angular velocity Ω.
- The stretching velocity of surface is expressed as $\check{v}_{1w} = b\check{x}$.
- Dust particles are taken as equally sized spheres.
- The density of dust and nanoparticles is considered constant throughout the flow field.
- Figure 1 geometrically illustrates the flow configuration.

Based on the above physical assumptions, the governing system is derived. The following presents a complete statement of the boundary layer problem to ensure mathematical clarity.

Governing system

The conservation of mass, momentum, and energy for steady nanofluid flow is governed by the following system of coupled and nonlinear equations[38,39,41]:

$$\frac{\partial \check{v}_1}{\partial \check{x}} + \frac{\partial \check{v}_2}{\partial \check{y}} + \frac{\partial \check{v}_3}{\partial \check{z}} = 0, \tag{1}$$

$$\check{v}_1 \frac{\partial \check{v}_1}{\partial \check{x}} + \check{v}_2 \frac{\partial \check{v}_1}{\partial \check{y}} + \check{v}_3 \frac{\partial \check{v}_1}{\partial \check{z}} - 2\Omega \check{v}_2 = \nu_{nf} \frac{\partial^2 \check{v}_1}{\partial \check{z}^2} - \frac{\nu_{nf}}{K_0} \check{v}_1 + \frac{KN}{\rho_{nf}} (\check{v}_{1p} - \check{v}_1) - F^* \check{v}_1^2, \tag{2}$$

$$\check{v}_1 \frac{\partial \check{v}_2}{\partial \check{x}} + \check{v}_2 \frac{\partial \check{v}_2}{\partial \check{y}} + \check{v}_3 \frac{\partial \check{v}_2}{\partial \check{z}} + 2\Omega \check{v}_1 = \nu_{nf} \frac{\partial^2 \check{v}_2}{\partial \check{z}^2} - \frac{\nu_{nf}}{K_0} \check{v}_2 + \frac{KN}{\rho_{nf}} (\check{v}_{2p} - \check{v}_2) - F^* \check{v}_2^2, \tag{3}$$

$$\left.\begin{aligned} \check{v}_1 \frac{\partial \check{T}}{\partial \check{x}} + \check{v}_2 \frac{\partial \check{T}}{\partial \check{y}} + \check{v}_3 \frac{\partial \check{T}}{\partial \check{z}} = \; & \frac{k_{nf}}{(\rho c_p)_{nf}} \frac{\partial^2 \check{T}}{\partial \check{z}^2} + \frac{\nu_{nf}}{(c_p)_{nf}} \left[\left(\frac{\partial \check{v}_1}{\partial \check{z}} \right)^2 + \left(\frac{\partial \check{v}_2}{\partial \check{z}} \right)^2 \right] \\ & - \frac{1}{(\rho c_p)_{nf}} \frac{\partial Q_r^*}{\partial \check{z}} - \frac{\rho_p (c_p)_f}{(\rho c_p)_{nf} \tau_T} (\check{T} - \check{T}_p) \end{aligned}\right\}, \tag{4}$$

for the dust-phase flow

$$\frac{\partial \check{v}_{1p}}{\partial \check{x}} + \frac{\partial \check{v}_{2p}}{\partial \check{y}} + \frac{\partial \check{v}_{3p}}{\partial \check{z}} = 0, \tag{5}$$

$$\check{v}_{1p} \frac{\partial \check{v}_{1p}}{\partial \check{x}} + \check{v}_{2p} \frac{\partial \check{v}_{1p}}{\partial \check{y}} + \check{v}_{3p} \frac{\partial \check{v}_{1p}}{\partial \check{z}} = 2\Omega \check{v}_{2p} + \frac{K}{m} (\check{v}_1 - \check{v}_{1p}), \tag{6}$$

$$\check{v}_{1p} \frac{\partial \check{v}_{2p}}{\partial \check{x}} + \check{v}_{2p} \frac{\partial \check{v}_{2p}}{\partial \check{y}} + \check{v}_{3p} \frac{\partial \check{v}_{2p}}{\partial \check{z}} + 2\Omega \check{v}_{1p} = \frac{K}{m} (\check{v}_2 - \check{v}_{2p}), \tag{7}$$

$$\check{v}_{1p} \frac{\partial \check{T}_p}{\partial \check{x}} + \check{v}_{2p} \frac{\partial \check{T}_p}{\partial \check{y}} + \check{v}_{3p} \frac{\partial \check{T}_p}{\partial \check{z}} = \frac{c_p}{c_m \tau_t} (\check{T} - \check{T}_p), \tag{8}$$

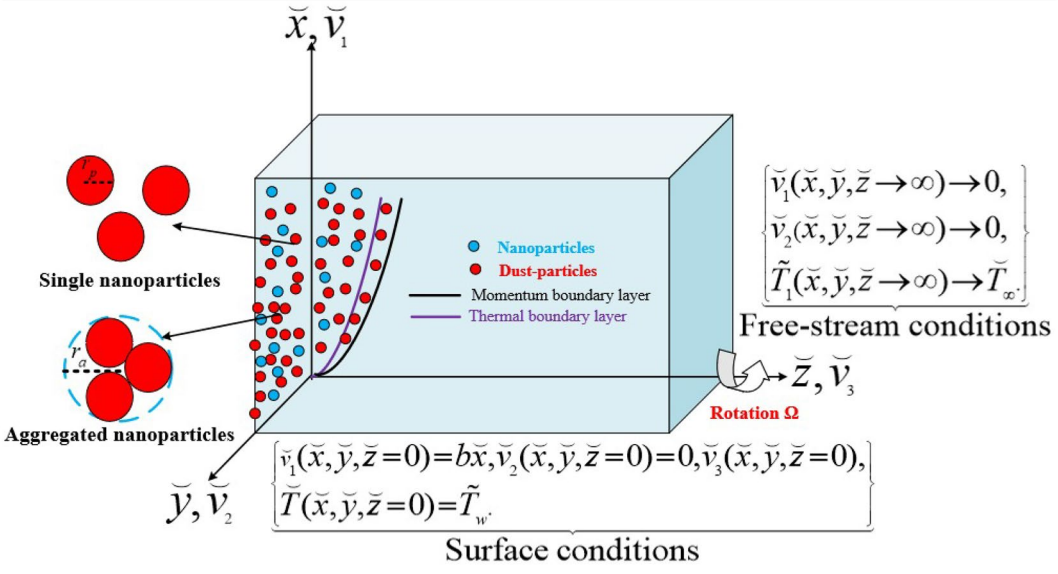

Fig. 1. Flow configuration.

where $(\check{v}_1, \check{v}_2, \check{v}_3)$ and $(\check{v}_{1p}, \check{v}_{2p}, \check{v}_{3p})$ represent the components of fluid and dust phase velocities, respectively, along the $(\check{x}, \check{y}, \check{z})$ directions. The fluid temperature is represented as $\check{T}$, while $\check{T}_p$ corresponds to the temperature of the dust phase. The terms ν_{nf}, k_{nf}, ρ_{nf}, and $(c_p)_{nf}$ indicate the kinematic viscosity, thermal conductivity, density, and heat capacity of the nanofluid, respectively. The angular velocity vector is $\Omega = [0, 0, \Omega]$. $F^* = \frac{C_b}{\check{x}\sqrt{K_0}}$ denotes the non-uniform inertia coefficient due to porous medium, K_0 represents permeability of the porous medium, and C_b stands for drag coefficient.

In high-temperature fluid systems, where transfer of energy occurs via conduction, convection, and electromagnetic emission, thermal radiation is crucial to the energy transfer process. To account for this mechanism, the radiative heat flux Q_r^* is introduced in energy equation. It denotes the net energy transfer rate resulting from thermal radiation. The Rosseland estimation is executed to model this heat flux[45], expressed as $Q_r^* = -\frac{4\alpha_1^*}{3m^*}\frac{\partial \check{T}^4}{\partial \check{z}}$, where the Stefan-Boltzmann constant is α_1^*, while m^* is the coefficient of mean absorption. The nonlinear term $\check{T}^4$ is expanded about ambient temperature $\check{T}_\infty$ using a Taylor series, assuming small temperature variations, as

$$\check{T}^4 = 4\check{T}_\infty^3 \check{T} - 3\check{T}_\infty^4.$$

Substituting this approximation yields the linearized form of the radiative heat flux[46]:

$$Q_r^* = -\frac{4\alpha_1^*}{3m^*}\frac{\partial \check{T}^4}{\partial \check{z}} = -\frac{16\alpha_1^*\check{T}_\infty^3}{3m^*}\frac{\partial \check{T}}{\partial \check{z}}. \tag{9}$$

The intermediate steps are presented in the Appendix. This formulation shows how radiation increases the dusty nanofluid's effective thermal conductivity, affecting heat transfer. This kind of analysis is very important for making systems that work at high temperatures, like solar collectors, nuclear cooling channels, and rotating energy devices, where radiative heat transfer is the main way heat moves.

Using Eq. (9) in Eq. (4), we get

$$\left.\begin{aligned} \check{v}_1\frac{\partial \check{T}}{\partial \check{x}} + \check{v}_2\frac{\partial \check{T}}{\partial \check{y}} + \check{v}_3\frac{\partial \check{T}}{\partial \check{z}} = \frac{k_{nf}}{(\rho c_p)}_{nf}\frac{\partial^2 \check{T}}{\partial \check{z}^2} + \frac{\nu_{nf}}{(c_p)}_{nf}\left[\left(\frac{\partial \check{v}_1}{\partial \check{z}}\right)^2 + \left(\frac{\partial \check{v}_2}{\partial \check{z}}\right)^2\right] \\ + \frac{1}{(\rho c_p)}_{nf}\frac{\partial}{\partial \check{z}}\left(\frac{16\alpha_1^*\check{T}_\infty^3}{3m^*}\frac{\partial \check{T}}{\partial \check{z}}\right) - \frac{\rho_p(c_p)_f}{(\rho c_p)_{nf}\tau_T}(\check{T} - \check{T}_p) \end{aligned}\right\}. \tag{10}$$

Boundary conditions

The associated boundary conditions are[33,47]:

$$\begin{cases} \check{v}_1 = \check{v}_{1w} = b\check{x}, \quad \check{v}_2 = 0, \quad \check{v}_3 = 0, \quad \check{T} = \check{T}_w, \quad \text{as} \quad \check{z} = 0, \\ \check{v}_1 \to 0, \ \check{v}_{1p} \to 0, \ \check{v}_2 \to 0, \ \check{v}_{2p} \to 0, \ \check{v}_{3p} \to \check{v}_3, \ \check{T} \to \check{T}_\infty, \check{T}_p \to \check{T}_\infty, \ \text{as} \quad \check{z} \to \infty, \end{cases} \tag{11}$$

here, $\check{T}_w$ is wall temperature, and $\check{T}_\infty$ represents ambient temperature.

Thermophysical properties

Experiments and theory suggest that nanofluids may demonstrate superior thermal conductivity compared to the base fluid. Enhancement occurs due to Brownian motion, interfacial effects, and significantly, nanoparticle aggregation, which create conductive networks that augment effective conductivity. In this study, we employ established mixture and aggregate models to simulate effective thermophysical properties, clearly delineating the underlying assumptions and their respective ranges of validity (Table 3).

The thermophysical properties of the nanofluid, considering nanoparticle aggregation, are defined as follows[48,49]:

The thermal properties associated with nanoparticle aggregation (represented by the subscript 'agg') are:

Properties	With aggregation	Without aggregation
Viscosity	$\mu_{nf} = \mu_f\left(1 - \frac{\phi_{agg}}{\phi_m}\right)^{-2.5\phi_m}$	$\mu_{nf} = \mu_f\left(1-\phi\right)^{-2.5}$
Density	$\rho_{nf} = \rho_f(1-\phi_{agg}) + \rho_s\phi_{agg}$	$\rho_{nf} = \rho_f\left(1-\phi\right) + \rho_s\phi$
Thermal conductivity	$k_{nf} = k_f\left(\frac{k_{agg}-2(k_f-k_{agg})\phi_{agg}+2k_f}{k_{agg}+(k_f-k_{agg})\phi_{agg}+2k_f}\right)$	$k_{nf} = k_f\left(\frac{k_s-2\phi(k_f-k_s)+2k_f}{k_s+\phi(k_f-k_s)+2k_f}\right)$
Heat capacity	$(\rho c_p)_{nf} = (\rho c_p)_f(1-\phi_{agg}) + (\rho c_p)_s\phi_{agg}$	$(\rho c_p)_{nf} = (1-\phi)\,(\rho c_p)_f + \phi(\rho c_p)_s$

Table 3. Thermophysical properties with and without the presence of nanoparticle aggregation.

$$\rho_{agg} = \rho_f(1-\phi_{int}) + \rho_s\phi_{int},$$
$$\phi_{int} = \left(\frac{R_{agg}}{R_p}\right)^{3-D},$$
$$\phi_{agg} = \frac{\phi}{\phi_{int}},$$
$$k_{agg} = \frac{k_f}{4}\left[\frac{k_s}{k_f}(3\phi_{int}-1) + (3(1-\phi_{int})-1) + \left(\frac{k_s}{k_f}(3\phi_{int}-1) + (3(1-\phi_{int})-1)^2 + 8\frac{k_s}{k_f}\right)^{0.5}\right],$$
$$(\rho c_p)_{agg} = (\rho c_p)_f(1-\phi_{int}) + (\rho c_p)_s\phi_{int}.$$

where ϕ_m, ϕ, ϕ_{int}, and ϕ_{agg} denote the maximum particle packing fraction, nanoparticle volume fraction, nanoparticle volume fraction within the aggregate, and effective particle volume fraction of aggregates, respectively. According to fractal theory, R_{agg} and R_p represent the radii of aggregates and primary nanoparticles, respectively. The ratio $\frac{R_{agg}}{R_p}$ is assumed to be 3.34 and the value of ϕ_m is 0.605. D is the fractal index, typically 1.8 for spherical particles[50,51] and the value of ϕ is 0.03.

Transformations

To streamline the coupled nonlinear PDEs that dictate boundary-layer motion, suitable similarity transformations are employed. These transformations diminish the dimensional complexity of the problem by transforming the system into a series of ordinary differential equations that preserve the fundamental physical attributes of the flow. Such transformations facilitate efficient numerical calculations and enhance understanding of the impacts of governing parameters. Similarity transformations are expressed as follows[41,52]

$$: \begin{cases} \eta = \check{z}\left(\frac{b}{\nu_f}\right)^{0.5}, \quad \check{v}_1 = b\check{x}F'(\eta), \ \check{v}_{1p} = b\check{x}F_p(\eta), \ \check{v}_2 = b\check{x}G(\eta), \ (\check{T}_w - \check{T}_\infty)\theta(\eta) = \check{T} - \check{T}_\infty, \\ (\check{T}_w - \check{T}_\infty)\theta_p(\eta) = \check{T}_p - \check{T}_\infty, \check{v}_{2p} = b\check{x}G_p(\eta), \quad \check{v}_3 = -\sqrt{b\nu_f}F(\eta), \quad \check{v}_{3p} = -\sqrt{b\nu_f}F_p(\eta). \end{cases} \tag{12}$$

Dimensionless system

Application of transformations given in (12) satisfies Eqs. (1) and (5) automatically and all other governing equations are transformed as:

$$\frac{\chi_1}{\chi_2}(F''' - K_pF') + 2\Gamma_rG - (1+F_r)F'^2 + FF'' - \frac{\Gamma_v\beta_v}{\chi_2}(F' - F_p') = 0, \tag{13}$$
$$\frac{\chi_1}{\chi_2}(G'' - K_pG) - 2\Gamma_rF - F_rG^2 + FG' - F'G - \frac{\Gamma_v\beta_v}{\chi_2}(G - G_p) = 0, \tag{14}$$
$$\frac{1}{\chi_4 P_r}(\chi_3 + Rd)\,\theta'' + F\theta' - \frac{\gamma_t\beta_t}{\chi_4}(\theta - \theta_p) + \frac{\chi_1}{\chi_4}E_c\left(F''^2 + G'^2\right) = 0, \tag{15}$$
$$F_pF_p'' - F_p'^2 + 2\Gamma_rG_p + \beta_v(F' - F_p') = 0, \tag{16}$$
$$F_pG_p' - G_pF_p' - 2\Gamma_rF_p' + \beta_v(G - G_p) = 0, \tag{17}$$
$$F_p\theta_p' - \beta_t\gamma_t(\theta_p - \theta) = 0. \tag{18}$$

The transformed boundary conditions are:

$$\begin{cases} G = 0, \quad F = 0, \quad F' = 1, \quad \theta = 1, \quad \text{for} \quad \eta = 0 \\ F_p' \to 0, \ F' \to 0, \ G \to 0, \quad \theta_p' \to 0, G_p \to 0, \ F_p = F \to 0, \ \text{for } \eta \to \infty. \end{cases} \tag{19}$$

To address the altered thermophysical characteristics of the nanofluid due to nanoparticle aggregation, various dimensionless factors are proposed. The terms $\chi_1 = \frac{\mu_{nf}}{\mu_f}$, $\chi_2 = \frac{\rho_{nf}}{\rho_f}$, $\chi_3 = \frac{k_{nf}}{k_f}$, and $\chi_4 = \frac{(\rho c_p)_{nf}}{(\rho c_p)_f}$ represent the nanofluid-base fluid viscosity, density, thermal conductivity, and heat capacity ratios. These parameters show how nanoparticle incorporation affects momentum and heat transfer. The dimensionless parameters involved in above equations are: the porosity parameter K_p, rotation parameter Γ_r, Forchheimer number F_r, radiation parameter Rd, Prandtl number P_r, Eckert number E_c, and dusty fluid parameters ($\gamma_t, \beta_t, \beta_v, \Gamma_v$). The dimensionless parameters are defined as follows:

$$\begin{cases} P_r = \frac{(\mu c_p)_f}{k_f}, \ \Gamma_r = \frac{\Omega}{b}, \ F_r = K_0^{-0.5}C_b, \quad K_p = \frac{\nu_f}{bK_0}, \\ \Gamma_v = \frac{mN}{\rho_f}, \quad \gamma_t = \frac{c_p}{c_m}, \quad \beta_v = \frac{K}{bm}, \\ \beta_t = \frac{1}{b\tau_t}, \quad Rd = \frac{16\alpha_1^*\check{T}_\infty^3}{3k_fm^*}, \quad E_c = \frac{\check{v}_{1w}^2}{(\check{T}_w - \check{T}_\infty)(c_p)_f}. \end{cases} \tag{20}$$

Their dimensionless nature is demonstrated in the Appendix.

Engineering quantities

Skin friction coefficient C_{f_x} and local Nusselt number N_{u_x} are defined as[39,40]:

$$C_{f_x} = \frac{\check{\tau}_w^x}{\check{v}_1^2 \rho_f}, \quad N_{u_x} = \frac{\check{x}\check{Q}_w}{k_f(\check{T}_w - \check{T}_\infty)}, \tag{21}$$

where $\check{\tau}_w^x$ is shear stress at wall and $\check{Q}_w$ denotes heat flux at wall.

$$\check{\tau}_w^x = \mu_{nf} \frac{\partial \check{v}_1}{\partial \check{z}}\bigg|_{\check{z}=0}, \quad \check{Q}_w = -\frac{k_f}{k_{nf}} \frac{\partial \check{T}}{\partial \check{z}}\bigg|_{\check{z}=0} + \frac{4\alpha_1^*}{3m^*} \frac{\partial \check{T}^4}{\partial \check{z}}\bigg|_{\check{z}=0}. \tag{22}$$

Using Eqs. (12) and (22), Eq. (21) takes the form:

$$Cf_x Re_x^{0.5} = \chi_1 F''(0), \quad Nu_x Re_x^{-0.5} = -\left(\chi_3 + \frac{4}{3}Rd\right)\theta'(0). \tag{23}$$

Local Reynolds number is given by $\sqrt{Re_x} = \frac{\check{x}\sqrt{\check{b}}}{\sqrt{\check{\nu}_f}}$.

Entropy analysis

A dusty nanofluid system generates entropy due to the irreversible effects of drag and interphase momentum exchange as well as the intricate interaction between the fluid and dust particle phases. Given the strong relationship between the production of entropy and energy dissipation, the basic goal of thermodynamic optimization is to minimize entropy generation. It is possible to measure irreversibilities in dusty flows and to account for the energy loss due to dust-fluid coupling and porous resistance by undertaking an entropy evaluation. Measuring entropy production helps identify inefficiencies that may cause system problems. This approach is analogous to detecting operational or process mechanism defects, and once recognized, system efficiency can be greatly improved.

Maximizing thermodynamic efficiency while limiting entropy formation is still a major goal in many industrial and technological domains. The depletion of global energy supplies has emphasized the need to optimize the processes of energy generation, transformation, and application, driving the advancement of sustainable technologies that prioritize efficiency[53]. The dimensional form of entropy generation rate E_{gen} is given by[35,53,54]:

$$E_{gen} = \underbrace{\frac{k_{nf}}{\check{T}_\infty^2}\left[1 + \frac{16\alpha_1^*\check{T}_\infty^3}{3m^* k_f}\right]\left(\frac{\partial \check{T}}{\partial \check{z}}\right)^2}_{\text{irreversibility of heat transfer}} + \underbrace{\frac{\mu_{nf}}{\check{T}_\infty}\left[\left(\frac{\partial \check{v}_1}{\partial \check{z}}\right)^2 + \left(\frac{\partial \check{v}_2}{\partial \check{z}}\right)^2\right]}_{\text{irreversibility of fluid friction}} + \underbrace{\frac{\mu_{nf}}{\check{T}_\infty K_0}\left(\check{v}_1^2 + \check{v}_2^2\right)}_{\text{irreversibility of porous medium}}. \tag{24}$$

Equation (24) reveals three main sources of entropy generation in dusty nanofluid: heat transfer due to temperature gradient, viscous dissipation resulting from interphase drag between dust and fluid particles, and flow resistance within the porous medium. The volumetric entropy generation rate *Ns*, defined as the ratio of E_{gen} to E_0, where $E_0 = \left(\frac{\check{T}_w - \check{T}_\infty}{\check{T}_\infty}\right)^2 \frac{bk_f}{\nu_f}$[53,54], represents the characteristic entropy generation. By using transformations (12), Eq. (24) becomes

$$Ns = \frac{E_{gen}}{E_0} = \chi_3 (1 + Rd)\,\theta'^2 + \chi_1 Br\delta\left(F''^2 + G'^2\right) + \chi_1 Br\delta K_p\left(F'^2 + G^2\right). \tag{25}$$

The detailed derivation of Eq. (24) and the reduction of Eq. (25) is given in the Appendix. Above, the dimensionless temperature difference parameter $\left(\delta = \frac{\check{T}_\infty}{\check{T}_w - \check{T}_\infty}\right)$ illustrates the temperature gradient over the boundary layer by comparing the ambient temperature to the surface temperature differential. It is a measure of the system's non-isothermality, which controls the rate of heat transfer from the surface to the fluid around it. The Brinkman number $\left(Br = \frac{\check{v}_{1w}^2 \mu_f}{\Delta \check{T} k_f}\right)$ shows the ratio of heat transfer due to viscous dissipation to heat transfer due to conduction. It measures how much of the overall energy loss is attributable to viscous heating as a result of friction between fluid particles and between phases. In dusty nanofluids, higher *Br* values signify increased viscous effects due to particle drag, thereby intensifying local entropy generation.

Quantifying the various entropy-generating components in a dusty nanofluid helps evaluate how dust particles alter energy dissipation within the boundary layer. The Bejan number defined mathematically as[7,55], is an important dimensionless number for this assessment.

$$Be = \frac{\text{Heat transfer entropy generation}}{\text{Total entropy generation}}, \tag{26}$$

non-dimensionalized form is as follows:

$$Be = \frac{\chi_3 \left(1 + Rd\right) \theta'^2}{Ns}. \tag{27}$$

Methodology

The resulting system of ordinary differential equations is highly nonlinear, making it difficult to acquire accurate analytical solutions. Therefore, robust numerical approaches are required to solve the system. To address this, the numerical solution for the nonlinear ODEs (13–18) subject to the boundary conditions (19) is obtained using the advanced boundary value problem solver bvp4c in MATLAB. This solver employs a collocation method with adaptive mesh refinement. The problem-solving flowchart is depicted in Fig. 2. The original boundary value problem (BVP) is systematically converted into an initial value problem (IVP) to make the numerical technique easier to apply. This transformation entails meticulously selecting and incorporating specific variables to ensure the procedure's efficacy. Error control and adaptive mesh refinement are included in the computational process and are gradually improved based on the computations' residuals[56]. The boundary layer region is determined for every set of parameter values, allowing for a thorough examination of the system's behavior. With a tolerance level of 10^{-6}, the numerical scheme converges, demonstrating the accuracy and dependability of the bvp4c solver.

The new variables are:

$$\begin{array}{llll} F = \hat{y}_1, & F' = \hat{y}_2, & F'' = \hat{y}_3, & G = \hat{y}_4, \\ G' = \hat{y}_5, & \theta = \hat{y}_6, & \theta' = \hat{y}_7, & F_p = \hat{y}_8, \\ F_p = \hat{y}_9, & G_p = \hat{y}_{10}, & \theta_p = \hat{y}_{11}. & \end{array}$$

The system of first-order ODEs is

$$\hat{y}_1' = \hat{y}_2, \tag{28}$$

$$\hat{y}_2' = \hat{y}_3, \tag{29}$$

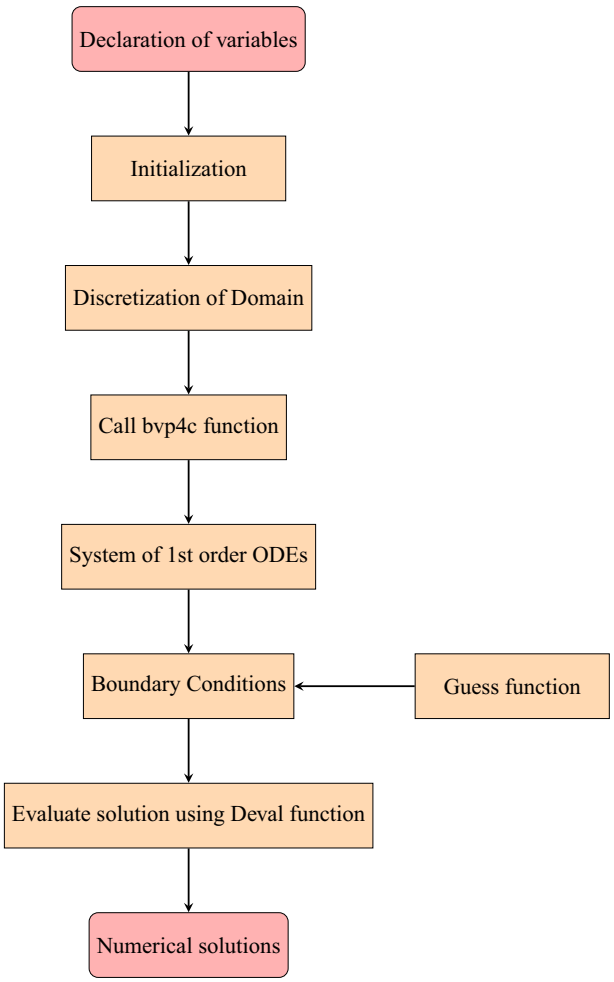

Fig. 2. Problem-solving flowchart for the present work.

$$\hat{y}_3' = K_p\hat{y}_2 - \frac{2\Gamma_r\hat{y}_4\chi_2}{\chi_1} + \frac{(1+F_r)\hat{y}_2^2\chi_2}{\chi_1} - \frac{\hat{y}_1\hat{y}_3\chi_2}{\chi_1} + \frac{\Gamma_v\beta_v\chi_2}{\chi_1}(\hat{y}_2 - \hat{y}_9), \tag{30}$$

$$\hat{y}_4' = \hat{y}_5, \tag{31}$$

$$\hat{y}_5' = K_p\hat{y}_4 + \frac{2\Gamma_r\hat{y}_2\chi_2}{\chi_1} + \frac{F_r\hat{y}_4^2\chi_2}{\chi_1} - \frac{\hat{y}_1\hat{y}_5\chi_2}{\chi_1} + \frac{\hat{y}_2\hat{y}_4\chi_2}{\chi_1} + \frac{\Gamma_v\beta_v(\hat{y}_4 - \hat{y}_{10})}{\chi_1}, \tag{32}$$

$$\hat{y}_6' = \hat{y}_7, \tag{33}$$

$$\hat{y}_7' = \frac{-\chi_4 P_r\hat{y}_1\hat{y}_7 + \gamma_t P_r\beta_t(\hat{y}_6 - \hat{y}_{11}) - \chi_1 P_r E_c\left(\hat{y}_3^2 + \hat{y}_5^2\right)}{\chi_3 + Rd}, \tag{34}$$

$$\hat{y}_8' = \hat{y}_9, \tag{35}$$

$$\hat{y}_9' = \frac{\hat{y}_9^2 - 2\Gamma_r\hat{y}_{10} - \beta_v(\hat{y}_2 - \hat{y}_9)}{\hat{y}_8}, \tag{36}$$

$$\hat{y}_{10}' = \frac{\hat{y}_9\hat{y}_{10} + 2\Gamma_r\hat{y}_9 - \beta_v(\hat{y}_4 - \hat{y}_{10})}{\hat{y}_8}, \tag{37}$$

$$\hat{y}_{11}' = \frac{\beta_t\gamma_t(\hat{y}_{11} - \hat{y}_6)}{\hat{y}_8}. \tag{38}$$

Transformed initial conditions are:

$$\begin{cases} \hat{y}_1(0) = 0, & \hat{y}_4(0) = 0, & \hat{y}_2(0) = 1, & \hat{y}_6(0) = 1, \\ \hat{y}_9(\infty) \to 0, & \hat{y}_2(\infty) \to 0, & \hat{y}_4(\infty) \to 0, \hat{y}_{11}(\infty) \to 0, \hat{y}_{10}(\infty) \to 0, \hat{y}_8(\infty) = \hat{y}_1(\infty) \to 0. \end{cases} \tag{39}$$

The computational domain was truncated at a suitable finite value of $\eta_\infty = 12$, which was determined numerically to adequately represent the asymptotic boundary conditions. The solver's convergence was governed by relative and absolute tolerance settings of 10^{-3} and 10^{-6}, respectively, ensuring that the maximum absolute residuals of the differential equations and boundary conditions satisfied the criterion $\max|\text{Residuals}| < \max(\text{AbsTol}, \text{RelTol} \times |\text{Solution}|)$. Mesh selection and error control were automatically handled by the algorithm based on the residual monitoring of the continuous solution. Different mesh sizes are shown by the relative error in Fig. 3. As the mesh is refined, the error goes down, reaching a minimum of 0.0002493 at a mesh size of 300. This shows that the chosen mesh achieves the best possible numerical accuracy and computational efficiency for this study.

Results and discussion

This section emphasizes interpreting the physical features of the embedded variables on velocity profiles ($F'(\eta)$, $F_p(\eta)$, $G(\eta)$ and $G_p(\eta)$), temperature profiles ($\theta(\eta)$ and $\theta_p(\eta)$), entropy generation (Ns), and Bejan number (Be), demonstrating the significance of nanoparticle aggregation. The findings are explained in detail via the graphic illustrations, clearly showing the observed trends. For limited cases, Tables 4 and 5 compare the skin friction and local Nusselt number with Rashid et al.[47]. These findings align with reported studies.

The default values of parameters and their ranges are selected based on their physical significance to encompass a broad spectrum of flow behaviors. The default values of physical parameters are: $P_r = 6.2$, $E_c = 0.1$, $\beta_v = 0.2$, $\beta_t = 0.1$, $\Gamma_v = 0.2$, and $\gamma_t = 0.2$. The porosity parameter ($K_p = 0.3{-}2.7$) shows the transition of highly dense medium to significantly permeable. This shows the influence on the degree of fluid

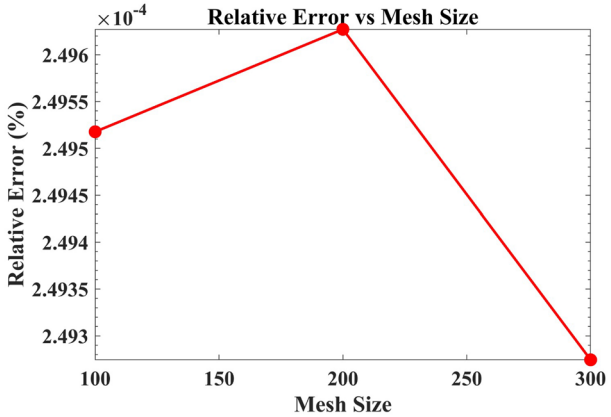

Fig. 3. Relative error for different mesh sizes.

Γ_r	K_p	F_r	Rashid et al.[40]	Our results	Error (%)
1	0.2	1	−1.58724	−1.5873	0.0038
2	0.2	1	−1.862267	−1.8622	0.0036
3	0.2	1	−2.10932	−2.1093	0.0009
0.5	0.1	1	−1.41806	−1.4182	0.0099
0.5	0.5	1	−1.53031	−1.5303	0.0007
0.5	0.5	1	−1.67153	−1.6716	0.0042
0.3	0.1	1	−1.36352	−1.3635	0.0015
0.3	0.1	2	−1.58502	−1.5850	0.0013
0.3	0.1	4	−1.96195	−1.9620	0.0025

Table 4. Comparison of skin friction with Rashid et al.[47] via Γ_r, K_p, and F_r, while neglecting other parameters.

K_p	Γ_r	P_r	Rashid et al.[40]	Our results	Error (%)
0	0.5	1	0.508972	0.50896	0.0024
1	0.5	1	0.485852	0.48585	0.0004
2	0.5	1	0.457520	0.45750	0.0044
0.2	0.1	1	0.542198	0.54216	0.0070
0.2	0.5	1	0.506965	0.50694	0.0049
0.2	0.9	1	0.467794	0.46769	0.0223
0.2	0.5	2	0.811336	0.811319	0.0021
0.2	0.5	3	1.064610	1.06465	0.0038
0.2	0.5	4	1.279790	1.27989	0.0078

Table 5. Comparison of Nusselt number with Rashid et al.[47] via K_p, Γ_r, and P_r, while neglecting other parameters.

penetration through the porous structure. The rotation parameter ($\Gamma_r = 0.5{-}2.5$) shows varying Coriolis effects, ranging from weak to strong rotational motion relevant to geophysical and industrial uses. The Forchheimer number ($F_r = 1{-}6$) measures the change from Darcy to non-Darcy regimes and includes inertial effects that are important at higher flow velocities. The radiation parameter ($Rd = 1{-}3$) corresponds to weak-to-moderate radiative heat transfer, ensuring thermal effects remain within practical operational limits. These ranges of parameters collectively ensure that both theoretical and realistic physical conditions are adequately represented in the analysis.

Velocity profiles

Figures 4, 5, and 6 demonstrate the influence of embedded parameters on axial and transverse velocities in both fluid and dust phases. Figure 4 illustrates the impact of rotation parameter Γ_r on axial velocities $(F'(\eta), F_p(\eta))$ and transverse velocities $(G(\eta), G_p(\eta))$ for both phases. Γ_r quantifies the rotational intensity acting through the Coriolis force, which redistributes momentum between velocity components. As Γ_r increases, the Coriolis force attenuates the axial flow while amplifying the transverse velocity, directing part of flow energy toward the perpendicular direction to maintain momentum balance. The maximum axial velocity occurs at $\Gamma_r = 0$, indicating pure stretching-driven flow. Physically, as Γ_r grows, the rotational influence dominates over the stretching rate, hindering fluid mobility along the x-direction and thereby thinning the boundary layer. Figure 4b also confirms that Γ_r promotes flow in the negative y-direction. At low Γ_r, flow follows the exponential decay pattern $-\eta \exp(-\eta)$, while oscillatory behavior emerges at larger Γ_r due to intensified Coriolis effects. Similar results are found by Lou et al.[38]. Figure 5 explains the variation in velocities caused by porosity parameter K_p. As K_p increases, the axial velocities of both phases decrease due to enhanced drag and viscous resistance introduced by the porous medium. Higher porosity signifies more flow resistance, which not only lower axial motion but also diminishes the transverse velocities. Figure 6 portrays the influence of Forchheimer number F_r on $F'(\eta)$, $F_p(\eta)$, $G(\eta)$ and $G_p(\eta)$. The Forchheimer number represents nonlinear inertial resistance in a porous medium. Both axial and transverse velocities decrease as F_r increases, suggesting that inertial drag increases the total resistance to motion by supplementing viscous friction. Rehman et al.[57] yielded analogous results for Figs. 5 and 6. Furthermore, Figs. 4, 5, and 6 show that when compared to the homogeneous nanoparticle model, the model that takes nanoparticle aggregation into account shows a discernible decrease in both velocity components. The aggregation raises the fluid's effective viscosity that slows down the axial and transverse fluid velocities by increasing flow resistance. In rotating filtration and cooling systems, where regulating the Coriolis-induced flow redistribution and porous drag aids in preserving the intended flow uniformity and efficiency, these velocity trends are extremely significant.

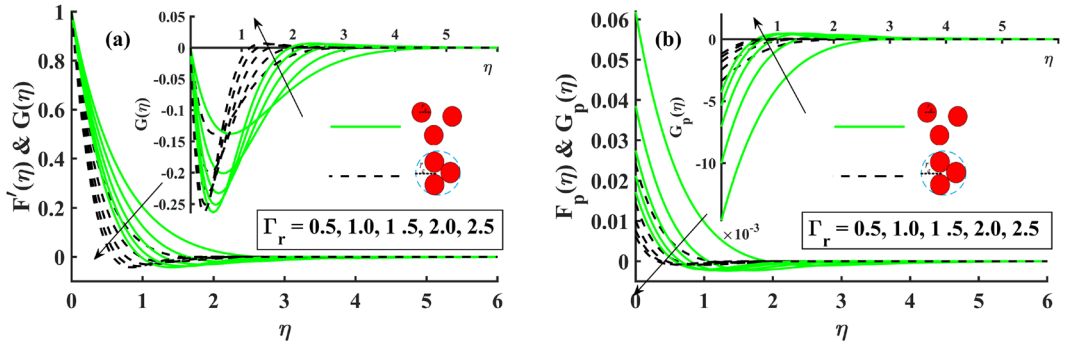

Fig. 4. Variation in velocity profiles against Γ_r.

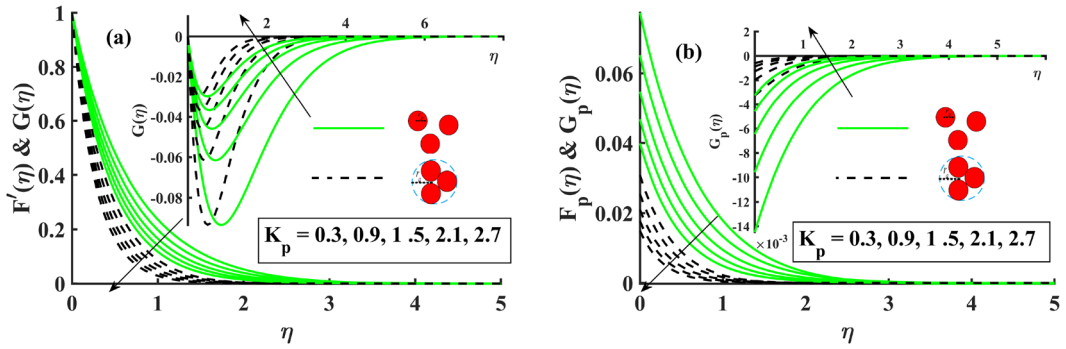

Fig. 5. Variation in velocity profiles against K_p.

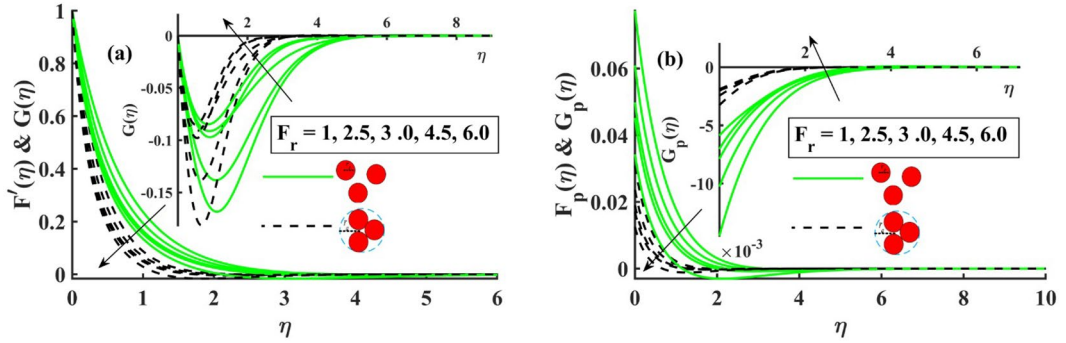

Fig. 6. Variation in velocity profiles against F_r.

Temperature profiles

The effects of different parameters on the temperature profiles $\theta(\eta)$ and $\theta_p(\eta)$ are shown in Figs. 7 and 8. Figure 7 shows that the temperature of both phases increases with the rotation parameter Γ_r. Enhanced rotation promotes heat exchange between the fluid and particles by strengthening shear interactions and energy dissipation. As a result, the system's total thermal energy rises as Γ_r. The findings of Lou et al.[38] echo this pattern for the rotation parameter. Higher porosity parameter K_p intensifies temperature because of increased viscous dissipation and frictional heating within the porous medium. Higher thermal fields are produced for both phases as a result of the increased resistance. Rehman et al.[57] also observed similar trends in their study. Figure 8a reveals a similar trend for the Forchheimer number F_r. The nonlinear flow resistance due to inertial effects results in increased energy dissipation as heat, hence elevating $\theta(\eta)$ and $\theta_p(\eta)$, supported by Rehman et al.[57]. Figure 8b indicates that the radiation parameter Rd substantially increases both $\theta(\eta)$ and $\theta_p(\eta)$. Since $Rd = \frac{16\alpha_1^* T^{*3}_\infty}{3k_f m^*}$, higher values of Rd reduce the mean absorption coefficient, enhancing radiative heat transfer and thus raising thermal energy in the boundary layer. This result mirrors the findings of Bhatti et al.[58]. Additionally, Figs. 7 and 8 show that the temperature profiles of the model accounting for nanoparticle aggregation are marginally elevated compared

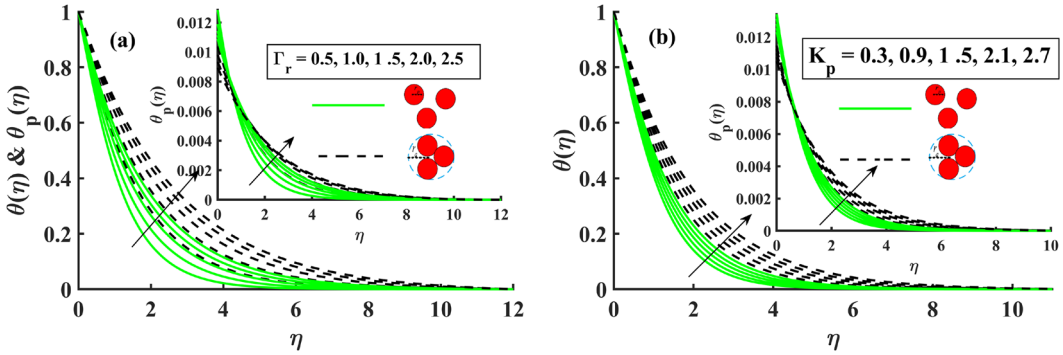

Fig. 7. Variation in temperature profiles against Γ_r and K_p.

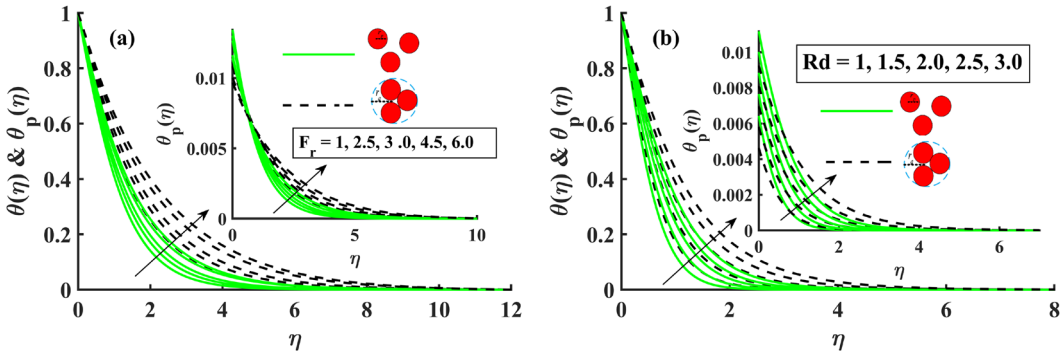

Fig. 8. Variation in temperature profiles against F_r and *Rd*.

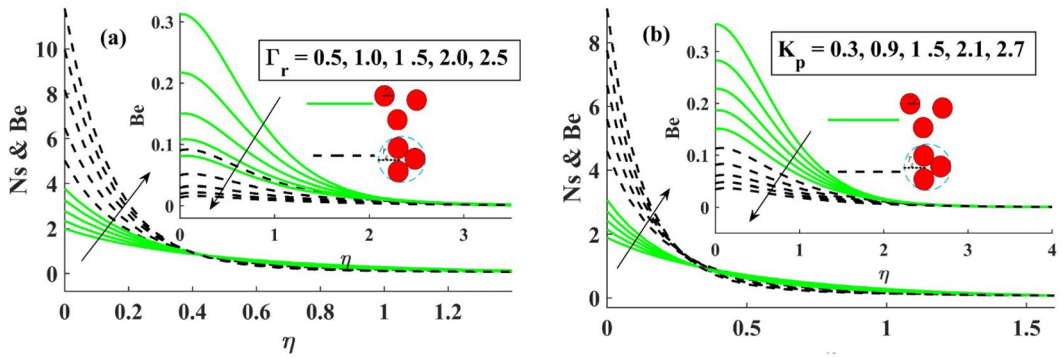

Fig. 9. Variation in *Ns* and *Be* against Γ_r and K_p.

to those of the homogeneous model, since aggregation amplifies interparticle interactions, hence enhancing the thermal conduction and storage capacity of the nanofluid[59,60]. Such temperature behavior is critical for designing rotational heat exchangers and electronic cooling equipment, since regulating radiative and viscous heating effects provides thermal stability and performance reliability.

Entropy generation and Bejan number

Figure 9 shows that increasing rotation and porosity parameters increase the entropy generation rate *Ns*, whereas the Bejan number *Be* exhibits an inverse response. The increase in entropy generation due to rotation results from enhanced Coriolis and centrifugal forces, which disrupt the orderly fluid motion and create more pronounced velocity gradients. These gradients enhance viscous dissipation, resulting in increased energy loss and thermodynamic irreversibility in both the fluid and dust phases. Concurrent with increased porosity, internal friction and interphase drag are amplified, resulting in enhanced mechanical energy conversion into heat via microscale interactions between dust particles and the fluid matrix. As a result, the system becomes increasingly dissipative, raising *Ns*. The Bejan number, representing a heat loss ratio to total entropy creation,

declines with rising porosity and rotation parameters. It in place of Tt signifies that the viscous effects prevail over thermal irreversibility as flow resistance escalates.

The impact of the Forchheimer number on *Ns* and *Be* is highlighted in Fig. 10a. Near the boundary layer, an increase in F_r strengthens inertial resistance and accelerates momentum diffusion, thereby increasing entropy formation through viscous dissipation. Away from the wall, the effect of inertia diminishes, resulting in a progressive decrease in energy dissipation and entropy generation. The reduction in *Be* with increased F_r indicates a transition from thermal to viscous entropy production, affirming that inertial drag amplifies mechanical irreversibility within the porous structure.

The influence of radiation parameter *Rd* on entropy and Bejan number is presented in Fig. 10b. As radiative heat transport strengthens, more energy is absorbed and re-emitted within the boundary layer, augmenting thermal gradients and promoting higher thermal entropy generation. This improvement happens because radiation makes fluid particles exchange energy more quickly, which speeds up thermal diffusion and irreversible heat transfer. But too much radiation can change the temperature distribution in the area, which can make conduction-dominated heat transfer near the wall less effective. Entropy production increases with radiation amplification because energy scatters more. It can lower conduction-driven entropy in some locations, causing the boundary layer's irreversibility to be unevenly distributed. These observed trends are in line with those of Hayat et al.[61].

Furthermore, the presence of nanoparticle aggregation amplifies entropy generation while lowering the Bejan number. Aggregated particles enhance effective viscosity and thermal coupling, hence amplifying both viscous and heating dissipation rates. Consequently, entropy generation increases due to intensified particle–fluid interactions and resistance to motion, while the decrease in *Be* indicates that viscous factors increasingly dictate the overall irreversibility of the system. Comprehending the roles of rotation, porosity, and radiation in entropy formation is essential for the design of energy-efficient porous systems, where the reduction of viscous irreversibility is crucial for enhanced thermal control.

Skin friction coefficient and the Nusselt number

The variations of the skin friction $Cf_x Re_x^{0.5}$ and local Nusselt number $Nu_x Re_x^{-0.5}$ are depicted in Fig. 11. The local Nusselt number characterizes the heat transfer rate, while skin friction coefficient quantifies the surface shear stress. As observed in Fig. 11a, increasing the Forchheimer's number and rotation parameter results in a more negative skin friction coefficient, signifying enhanced opposing shear at the wall. This trend results from increased inertial and resistive forces that amplify near-wall momentum retardation in the porous medium. Non-aggregated nanoparticles, due to their uniform dispersion, promote smoother momentum transfer with the base fluid, resulting in a comparatively less negative wall shear than their aggregated counterparts. As seen in Fig. 11b, non-aggregated nanoparticles exhibit superior heat transfer performance compared to aggregated ones owing to their uniform dispersion and larger effective surface area, which promote enhanced thermal conduction. Ali et al.[49] validate these findings. It shows that preventing clustering of nanoparticles markedly increases the Nusselt number despite the absence of aggregation-induced microchannels often thought to aid heat convection. This improved thermal response of non-aggregated model highlights the crucial role of nanoparticle stability in achieving efficient energy transport in rotating nanofluid systems. Conversely, increasing F_r and Γ_r reduces the Nusselt number by intensifying flow resistance and disturbing the thermal boundary layer, thereby weakening convective heat transport. These findings emphasize the necessity of preserving nanoparticle dispersion and reducing flow resistance in practical applications such as nuclear cooling systems and high-speed rotating machinery, where the increase of heat transfer directly influences operational safety and efficiency.

Conclusion

This study examined the nonlinear radiative flow and entropy generation in a rotating dusty nanofluid system, incorporating the combined effects of nanoparticle aggregation, Coriolis effects, Darcy–Forchheimer drag, and viscous dissipation. The governing PDEs were reduced to nonlinear ODEs via similarity transformations and solved using MATLAB's built-in bvp4c. Main findings drawn from this study are

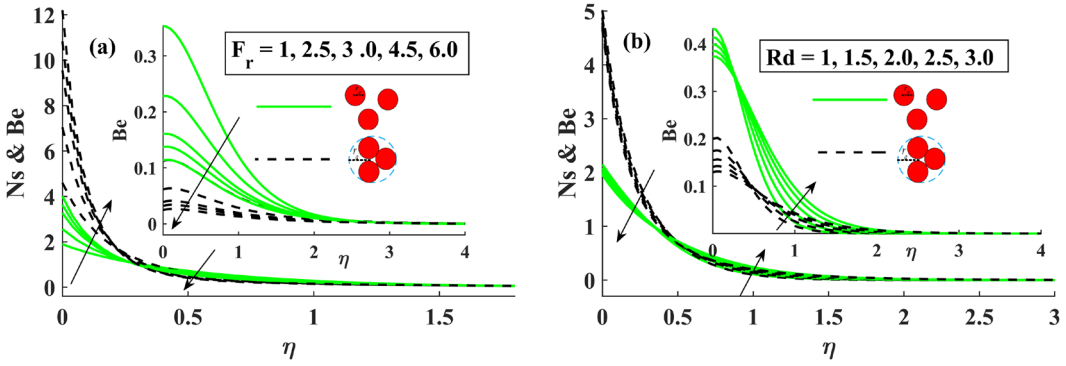

Fig. 10. Variation in *Ns* and *Be* against F_r and *Rd*.

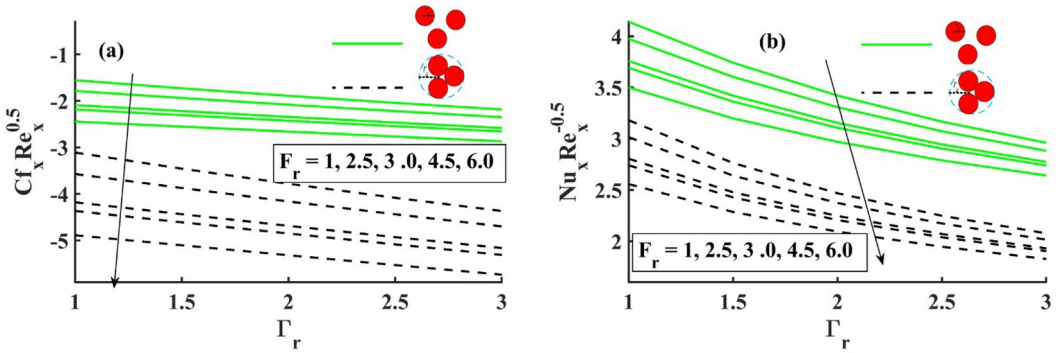

Fig. 11. Variation in $Cf_x Re_x^{0.5}$ and $Nu_x Re_x^{-0.5}$ against F_r and Γ_r.

- Nanoparticle aggregation reduces both axial and transverse velocities due to increased drag. However, it enhances temperature distribution and thermal conductivity, which can be useful in high-temperature applications like compact cooling systems and rotating thermal exchangers.
- Aggregation reduces the Nusselt number nearly 20% in the aggregated case as compared to non-aggregated one, indicating reduced heat transfer efficiency due to clusters.
- The Bejan number decreases by about 15% in the aggregated case relative to non-aggregated case, indicating diminished entropy generation.
- Stronger Coriolis effects suppress flow mobility but thicken the thermal boundary layer. It signifies that rotational intensity helps in flow regulation and heat dispersion in rotating filtration and energy systems.
- Radiation intensifies temperature and entropy generation, elevating the Bejan number, which shows its significance in high-temperature rotating configurations.
- Increasing porosity and Forchheimer number increase thermal boundary layer and entropy generation while lowering momentum and Bejan number. These characteristics are valuable in designing energy-efficient porous rotating systems with controlled permeability and inertial resistance.

Limitations and future research directions

The current model exclusively accounts for steady, laminar, and incompressible flow, whereas real-world systems often exhibit unstable or turbulent conditions that influence flow and heat transfer. Linear drag and energy exchange variables model the dust-fluid interaction without including interparticle collisions or dust-dust interactions, which could affect dispersion in dense or strongly rotating regimes. The magnetic field is assumed to be uniform and perpendicular to the flow; however, actual configurations typically exhibit nonuniform or inclined fields. The presumption of homogeneous aggregate size overlooks polydispersity that alters viscosity and conductivity. The numerical method appears dependable; nonetheless, experimental confirmation would enhance its expected reliability.

Future research may expand the current model to encompass unsteady or transient regimes. The framework can be expanded to elucidate intricate rheological phenomena in hybrid or tri-hybrid dusty nanofluids. Hall currents, nonuniform magnetic fields, and electromagnetohydrodynamic interactions would enhance physical realism. Incorporation of variable particle sizes and thermal nonequilibrium between dust and fluid is feasible. Experimental validation and sophisticated computational techniques, such as finite element method, could enhance precision. The research of entropy formation must include heat generation, chemical processes, and other irreversibilities to enhance the understanding of thermodynamic performance.

Data availability

All the data used during this study is accessible within the manuscript.

Received: 30 August 2025; Accepted: 6 November 2025
Published online: 27 November 2025

References

1. Saffman, P. G. On the stability of laminar flow of a dusty gas. *J. Fluid Mech.* **13**(1), 120–128 (1962).
2. Ezzat, M. A., El-Bary, A. A. & Morsey, M. M. Space approach to the hydro-magnetic flow of a dusty fluid through a porous medium. *Comput. & Math. Appl.* **59**(8), 2868–2879 (2010).
3. Dey, D. & Chutia, B. Dusty nanofluid flow with bioconvection past a vertical stretching surface. *J. King Saud Univ.-Eng. Sci.* **34**(6), 375–380 (2022).
4. Sharif, H. et al. Numerical investigation of dusty tri-hybrid Ellis rotating nanofluid flow and thermal transportation over a stretchable Riga plate. *Sci. Rep.* **13**(1), 14272 (2023).
5. Bejan, A. A study of entropy generation in fundamental convective heat transfer. *J. Heat Transf.* **101**(4), 718–725 (1979).
6. Bejan, A. & Kestin, J. Entropy generation through heat and fluid flow. *J. Appl. Mech.* **50**, 475–475 (1983).
7. Bejan, A. Entropy generation minimization: The new thermodynamics of finite-size devices and finite-time processes. *J. Appl. Phys.* **79**(3), 1191–1218 (1996).
8. Kumar, M., Kaswan, P., & Kumari, M. Numerical simulation of entropy generation analysis of MHD hybrid-nanofluid flow with nonlinear thermal radiation and melting heat transfer. *Spec. Top. Rev. Porous Media Int. J.* **13**(6), (2022).

9. Agrawal, R. & Kaswan, P. Entropy generation minimization of Ag-Fe_3O_4/water-ethylene glycol squeezed hybrid nanofluid flow between parallel disks. *Int. J. Numer. Methods Heat Fluid Flow* **33**(1), 65–95 (2023).
10. Khan, S. A., Hayat, T., Razaq, A. & Momani, S. Entropy optimized flow subject to variable fluid characteristics and convective conditions. *Alex. Eng. J.* **86**, 616–630 (2024).
11. Kumar, M., Kaswan, P., Kumari, M., Ahmad, H. & Askar, S. Cattano Christov double diffusion model for third grade nanofluid flow over a stretching Riga plate with entropy generation analysis. *Heliyon* **10**(10), e30188 (2024).
12. Kumar, M., Kaswan, P. & Kumari, M. Entropy generation analysis of microrotating Casson's nanofluid with Darcy-Forchheimer porous media using a neural computing based on Levenberg–Marquardt algorithm. *Int. J. Numer. Methods Heat Fluid Flow* **34**(6), 2285–2320 (2024).
13. Yusuf, A., Bhatti, M. M. & Khalique, C. M. Computational study of the thermophysical properties of graphene oxide/vacuum residue nanofluids for enhanced oil recovery. *J. Therm. Anal. Calorim.* **150**(1), 771–783 (2025).
14. Long, X., Guo, Y., Su, Y., Siow, K. S. & Chen, C. Unveiling the damage evolution of SAC305 during fatigue by entropy generation. *Int. J. Mech. Sci.* **244**, 108087 (2023).
15. Choi, S. U. & Eastman, J. A. *Enhancing thermal conductivity of fluids with nanoparticles* (No. ANL/MSD/CP-84938; CONF-951135-29). (Argonne National Lab. (ANL), Argonne, 1995).
16. Long, X., Chong, K., Su, Y., Du, L. & Zhang, G. Connecting the macroscopic and mesoscopic properties of sintered silver nanoparticles by crystal plasticity finite element method. *Eng. Fract. Mech.* **281**, 109137 (2023).
17. He, D., Xu, H., Wang, M. & Wang, T. Transmission and dissipation of vibration in a dynamic vibration absorber-roller system based on particle damping technology. *Chin. J. Mech. Eng.* **37**(1), 108 (2024).
18. Darvesh, A. et al. Rheology of variable viscosity-based mixed convective inclined magnetized cross nanofluid with varying thermal conductivity. *Appl. Sci.* **12**(18), 9041 (2022).
19. Abbas, N., Shatanawi, W. & Taqi, A. M. Thermodynamic study of radiative chemically reactive flow of induced MHD sutterby nanofluid over a nonlinear stretching cylinder. *Alex. Eng. J.* **70**, 179–189 (2023).
20. Shah, S. Z. H. et al. Thermal transport exploration of ternary hybrid nanofluid flow in a non-Newtonian model with homogeneous-heterogeneous chemical reactions induced by vertical cylinder. *Adv. Mech. Eng.* **16**(5), 16878132241252228 (2024).
21. Akbar, A. A. et al. Magnetized heat transfer visualization through computational modeling of third-grade fluid via exponentially stretching cylinder. *Mod. Phys. Lett. B* **33**, 2450334 (2024).
22. Oni, M. O. et al. Theory of conjugate mixed convection flow of hybridized ethylene glycol based nanoparticles with Joule heating. *J. Therm. Anal. Calorim.* **150**, 1–13 (2025).
23. Yusuf, A., Bhatti, M. M. & Ellahi, R. Study of ionic water/graphene nanofluids in solar panels under the effects of thermal radiation and slip conditions using experimental data. *Int. Commun. Heat Mass Transf.* **164**, 108845 (2025).
24. Hussain, M. et al. Characterization of thermal buoyancy forces and suction on bioconvective magnetohydrodynamic dusty nanofluid flow over a stretching surface. *Mod. Phys. Lett. B* **39**, 2550209 (2025).
25. Zhu, H. T., Zhang, C. Y., Tang, Y. M. & Wang, J. X. Novel synthesis and thermal conductivity of CuO nanofluid. *J. Phys. Chem. C* **111**(4), 1646–1650 (2007).
26. Liu, M. S., Lin, M. C. C., Tsai, C. Y. & Wang, C. C. Enhancement of thermal conductivity with Cu for nanofluids using chemical reduction method. *Int. J. Heat Mass Transf.* **49**(17–18), 3028–3033 (2006).
27. Wang, B. X., Zhou, L. P. & Peng, X. F. A fractal model for predicting the effective thermal conductivity of liquid with suspension of nanoparticles. *Int. J. Heat Mass Transf.* **46**(14), 2665–2672 (2003).
28. Liu, X. C., Sun, Y. F., Morisada, Y. & Fujii, H. Dynamics of rotational flow in friction stir welding of aluminum alloys. *J. Mater. Process. Technol.* **252**, 643–651 (2018).
29. Bilal, M. & Ramzan, M. Hall current effect on unsteady rotational flow of carbon nanotubes with dust particles and nonlinear thermal radiation in Darcy-Forchheimer porous media. *J. Therm. Anal. Calorim.* **138**(5), 3127–3137 (2019).
30. Zafar, A. A., Riaz, M. B. & Asjad, M. I. Unsteady rotational flow of fractional Maxwell fluid in a cylinder subject to shear stress on the boundary. *Punjab Univ. J. Math.* **50**(2), 21 (2020).
31. Mishra, S. & Mondal, H. Rotational microorganism magneto-hydrodynamic nanofluid flow with Lorentz and Coriolis force on moving vertical plate. *BioNanoScience* **14**, 1–18 (2024).
32. Jat, K., Sharma, K., Choudhary, P. & Soni, P. Bioconvection of a radiating and reacting nanofluid flow past a nonlinear stretchable permeable sheet in a porous medium. *J. Biol. Phys.* **51**(1), 8 (2025).
33. Shaheen, N., Ramzan, M., Alshehri, A., Shah, Z. & Kumam, P. Soret-Dufour impact on a three-dimensional Casson nanofluid flow with dust particles and variable characteristics in a permeable media. *Sci. Rep.* **11**(1), 14513 (2021).
34. Jat, K., Sharma, K., Choudhary, P. & Soni, P. Entropy generation analysis of couple stress Casson fluid flow through non-permeable stretching channel. *Eur. Phys. J. Spec. Top.* 1–20 (2025).
35. Seth, G. S., Kumar, R. & Bhattacharyya, A. Entropy generation of dissipative flow of carbon nanotubes in rotating frame with Darcy–Forchheimer porous medium: A numerical study. *J. Mol. Liq.* **268**, 637–646 (2018).
36. Tlili, I., Ramzan, M., Kadry, S., Kim, H. W. & Nam, Y. Radiative MHD nanofluid flow over a moving thin needle with entropy generation in a porous medium with dust particles and Hall current. *Entropy* **22**(3), 354 (2020).
37. Yusuf, A., Khan, S. U., Hassan, M., Bhatti, M. M. & Öztop, H. F. Heat transfer optimization of MWCNT-Al_2O_3 hybrid nanofluids under convective and irreversible effects. *J. Umm Al-Qura Univ. Appl. Sci.* 1–15, (2025).
38. Lou, Q. et al. Micropolar dusty fluid: Coriolis force effects on dynamics of MHD rotating fluid when Lorentz force is significant. *Mathematics* **10**(15), 2630 (2022).
39. Ullah, I., Hayat, T., Aziz, A. & Alsaedi, A. Significance of entropy generation and the Coriolis force on the three-dimensional non-Darcy flow of ethylene-glycol conveying carbon nanotubes (SWCNTs and MWCNTs). *J. Non-Equilib. Thermodyn.* **47**(1), 61–75 (2022).
40. Darvesh, A. et al. Thermal diffusivity of inclined magnetized Cross fluid with temperature dependent thermal conductivity: Spectral relaxation scheme. *Discov. Appl. Sci.* **6**(3), 117 (2024).
41. Hussain, M., Ali, B., Awan, A. U., Alharthi, M. & Alrashedi, Y. Role of nanoparticle radius for heat transfer optimization in MHD dusty fluid across stretching sheet. *J. Therm. Anal. Calorim.* **149**(24), 15179–15192 (2024).
42. Ali, L. et al. Insight into significance of thermal stratification and radiation on dynamics of micropolar water based TiO_2 nanoparticle via finite element simulation. *J. Mater. Res. Technol.* **19**, 4209–4219 (2022).
43. Alanazi, M. M. et al. Significance of ternary hybrid nanoparticles on the dynamics of nanofluids over a stretched surface subject to gravity modulation. *Mathematics* **11**(4), 809 (2023).
44. Alanazi, M. M. et al. Numerical computation of hybrid morphologies of nanoparticles on the dynamic of nanofluid: The case of blood-based fluid. *Axioms* **12**(2), 163 (2023).
45. Brewster, M. Q. *Thermal radiative transfer and properties* (Wiley, 1992).
46. Datti, P. S., Prasad, K. V., Abel, M. S. & Joshi, A. MHD visco-elastic fluid flow over a non-isothermal stretching sheet. *Int. J. Eng. Sci.* **42**(8–9), 935–946 (2004).
47. Rashid, S., Hayat, T., Qayyum, S., Ayub, M. & Alsaedi, A. Three-dimensional rotating Darcy-Forchheimer flow with activation energy. *Int. J. Numer. Methods Heat Fluid Flow* **29**(3), 935–948 (2019).
48. Chen, H., Ding, Y., He, Y. & Tan, C. Rheological behaviour of ethylene glycol based titania nanofluids. *Chem. Phys. Lett.* **444**(4–6), 333–337 (2007).

49. Ali, B. et al. Significance of nanoparticles aggregation on the dynamics of rotating nanofluid subject to gyrotactic microorganisms, and Lorentz force. *Sci. Rep.* **12**(1), 16258 (2022).
50. Ellahi, R., Hassan, M. & Zeeshan, A. Aggregation effects on water base Al_2O_3—nanofluid over permeable wedge in mixed convection. *Asia-Pac. J. Chem. Eng.* **11**(2), 179–186 (2016).
51. Mahanthesh, B. & Thriveni, K. Nanoparticle aggregation effects on radiative heat transport of nanoliquid over a vertical cylinder with sensitivity analysis. *Appl. Math. Mech.* **42**, 331–346 (2021).
52. Mustafa, M., Hayat, T. & Alsaedi, A. Rotating flow of Maxwell fluid with variable thermal conductivity: An application to non-Fourier heat flux theory. *Int. J. Heat Mass Transf.* **106**, 142–148 (2017).
53. Awan, A. U. et al. Computational analysis of entropy generation in EMHD micropolar dusty fluid flow incorporating esterification process. *Sci. Rep.* **15**(1), 30146 (2025).
54. Muhammad, R., Khan, M. I., Jameel, M. & Khan, N. B. Fully developed Darcy-Forchheimer mixed convective flow over a curved surface with activation energy and entropy generation. *Comput. Methods Programs Biomed.* **188**, 105298 (2020).
55. Jarwal, V. K., Choudhary, S., Sharma, K. & Choudhary, P. Modeling and analysis of entropy in MHD unsteady flow of water-based nanofluids with carbon nanoparticles. *Discov. Appl. Sci.* **7**(7), 686 (2025).
56. Choudhary, P., Loganathan, K., Jat, K., Sharma, K. & Eswaramoorthi, S. Shape factor analysis of water and aluminium oxide nanoparticles in a porous medium with slip effects. *Chem. Phys. Impact* **10**, 100882 (2025).
57. Rehman, S. U. et al. The Casson dusty nanofluid: Significance of Darcy–forchheimer law, magnetic field, and non-Fourier heat flux model subject to stretch surface. *Mathematics* **10**(16), 2877 (2022).
58. Bhatti, M. M., Zeeshan, A., Ijaz, N., Bég, O. A. & Kadir, A. Mathematical modelling of nonlinear thermal radiation effects on EMHD peristaltic pumping of viscoelastic dusty fluid through a porous medium duct. *Eng. Sci. Technol., Int. J.* **20**(3), 1129–1139 (2017).
59. Wei, W. et al. Fractal analysis of the effect of particle aggregation distribution on thermal conductivity of nanofluids. *Phys. Lett. A* **380**(37), 2953–2956 (2016).
60. Chen, H., Witharana, S., Jin, Y., Kim, C. & Ding, Y. Predicting thermal conductivity of liquid suspensions of nanoparticles (nanofluids) based on rheology. *Particuology* **7**(2), 151–157 (2009).
61. Hayat, T. et al. Entropy generation in Darcy-Forchheimer bidirectional flow of water-based carbon nanotubes with convective boundary conditions. *J. Mol. Liq.* **265**, 629–638 (2018).

Acknowledgements

The authors extend their appreciation to the Deanship of Research and Graduate Studies at King KhalidUniversity for funding this work through Large Research Project under grant number RGP2/130/46.

Author contributions

B.A.: Conceptualization, Validation. M.H.: Formal Analysis, writing–original draft preparation. A. U. A.: Supervision, writing–review and editing. N.A.A.: Data curation, Resources. F.G.: Methodology, Software. D.M.G.: Resources, Investigation. S.N.: Investigation, visualization.

Funding

No funding is available for paying the article processing charges (APC).

Declaration

Competing interests

The authors have no conflict of interest to declare.

Ethical approval

The authors affirm their commitment to ethical standards.

Additional information

Supplementary Information The online version contains supplementary material available at https://doi.org/10.1038/s41598-025-27894-x.

Correspondence and requests for materials should be addressed to D.M.G.